A BIDOMAIN MODEL OF THE VENTRICULAR SPECIALIZED CONDUCTION SYSTEM OF THE HEART*

R. M. BORDAS[†], K. GILLOW[‡], D. GAVAGHAN[§], B. RODRIGUEZ[¶], AND D. KAY[§]

Abstract. An efficient bidomain model of electrical activity in cardiac specialized conduction system fibers is developed and applied to a geometric model of the specialized conduction system and the ventricles. The bidomain model allows the impact of externally applied electric fields on the specialized conduction system to be studied. To model this system, the three-dimensional bidomain equations for a fiber are reduced to one-dimensional equations governing electrical propagation by averaging over the fiber cross section. The one-dimensional equations are coupled to the surrounding three-dimensional extracellular electrical field to allow their use in defibrillation studies. A finite element method, with semi-implicit time stepping, is developed to numerically solve the equations. Current flow through fiber branch points is governed by Kirchhoff's law and imposed directly in a weak formulation of the equations for use with the finite element method. Coupling between intracellular potential in distal system Purkinje fibers and the myocardium at discrete Purkinje-ventricular junctions is modelled using a resistor model. Simulations of electrical activation through a geometric model of the specialized conduction system are presented. The simulations demonstrate physiologically realistic activation sequences under sinus rhythm and the impact of a large externally applied extracellular field on the specialized conduction system.

Key words. cardiac, specialized conduction system, electrophysiology, modelling, Purkinje, bidomain, monodomain, Purkinje-ventricular junctions, branch point

AMS subject classifications. 92C30, 93A30, 35K57

DOI. 10.1137/11082796X

1. Introduction. The ventricular specialized conduction system consists of a network of thin fibers that are electrically isolated from the myocardium. The function of the system is to ensure the coordinated electrical activation of the ventricles; this is critical to the overall function of the heart. Under normal sinus rhythm, electrical activity in the heart originates in the sino-atrial node, from which it propagates to the atrioventricular node and from there propagates toward the ventricles through the bundle of His, bundle branches, and finally into the Purkinje fiber network. The Purkinje fiber network electrically activates the myocardium at discrete Purkinje-ventricular (PV) junctions situated in the endocardium [35]. While essential to ventricular function, the specialized conduction system is often neglected in cardiac electrophysiology models [30, 31]. Furthermore, the specialized conduction

---

†Corresponding author. Computational Biology Group, Department of Computer Science, University of Oxford, Oxford OX1 3QD, UK (rafel.bordas@cs.ox.ac.uk). The research of this author was supported through an EPSRC funded Life Sciences Doctoral Training Centre studentship (grant EP/E501605/1) and an industrial sponsorship award funded by Fujitsu Laboratories of Europe Ltd.
‡Numerical Analysis Group, Oxford University Mathematical Institute, Oxford OX1 3LB, UK (kathryn.gillow@maths.ox.ac.uk).
§Computational Biology Group, Department of Computer Science, University of Oxford, Oxford OX1 3QD, UK (david.gavaghan@cs.ox.ac.uk, david.kay@cs.ox.ac.uk).
¶Computational Biology Group, Department of Computer Science, University of Oxford, Oxford OX1 3QD, UK (blanca@cs.ox.ac.uk). The research of this author was supported by a UK Medical Research Council (MRC) Career Development Award (grant G0700278).

system has been implicated as a key player in a number of pathologies leading to ventricular fibrillation [32].

Electrical activity in the heart is typically modelled using the bidomain equations [19]. The bidomain model consists of a system of two partial differential equations that model cardiac tissue as a homogenized domain consisting of both the intra- and extracellular spaces. The potential difference between the two spaces drives an ionic current across the cell membrane that separates them. The ionic current is calculated using an electrophysiology cell model, typically described by a system of ordinary differential equations. The numerical solution of the bidomain equations is usually calculated using the finite element method [7, 18, 40, 44]. However, a discretization of the whole heart with a typical node spacing of 250 μm generates a mesh with millions of nodes, and the solution of the bidomain equations on such a mesh is highly computationally expensive. This led to the development of the monodomain approximation of the bidomain equations. The monodomain model explicitly represents only the potential difference between the intra- and extracellular space and is more computationally tractable than the bidomain equations. Monodomain models allow propagation studies and can produce realistic activation patterns. However, monodomain models have limitations when compared to bidomain models; they do not permit currents in the extracellular domain to influence the transmembrane potential and transmembrane ionic currents. This precludes the use of monodomain models in defibrillation studies.

There have been several modelling studies aimed at increasing the understanding of the function of the specialized conduction system. Due to the small scale nature of the specialized conduction system and the computational difficulties discussed above, the system is typically modelled as a one-dimensional domain coupled to a three-dimensional representation of the ventricles. As a result, mathematical studies of this system have almost exclusively used a monodomain model of electrical activation [1, 4, 22, 26, 36, 37]. Few one-dimensional bidomain models of the specialized conduction system have previously been developed. One such model was developed specifically to model saw-tooth effects in a specialized conduction system geometry based on descriptions in the literature [41]. Another study, featuring a human heart and a torso model, embedded Purkinje fibers into a bidomain model [43]. Neither work explains in detail how the governing equations for the one-dimensional fibers or the coupling with the surrounding extracellular domain were derived. In both cases, the specialized conduction system is assumed not to affect the extracellular field. This precludes using the models to study how activation in the specialized conduction system may effect an electrocardiogram.

The aim of this work is to provide bidomain equations for a one-dimensional representation of the specialized conduction system coupled to a three-dimensional bidomain model of the ventricles. Two possible approaches exist to create a one-dimensional bidomain model of a specialized conduction system fiber that is compatible with a three-dimensional bidomain ventricular model:

- Derive a one-dimensional bidomain model by direct homogenization of a cellular representation. In order for the model to be compatible with a bidomain model of ventricular tissue, the assumptions used during homogenization must match those of the bidomain model as far as possible.
- Derive a one-dimensional bidomain model from a three-dimensional bidomain representation of the fiber making minimal assumptions and retaining as many features of the original model as possible.

The first approach would mirror the derivation of the three-dimensional bidomain equations [24]. It could also yield further insight into the conductivity in the specialized conduction system fibers given the distribution of myocytes using the techniques developed in [29]. However, in this work we take the latter approach: a one-dimensional bidomain model of a specialized conduction system fiber is derived from a corresponding three-dimensional bidomain model. We choose this option to ensure that our one-dimensional model is as close as possible to the three-dimensional model of ventricular tissue to which we will couple it. Previous work exists that takes this approach, most notably [25] and [15, 16]. However, the focus of those works was simulating propagation in a single fiber bundle, not embedding a one-dimensional model of the entire specialized conduction system into the ventricles.

By integrating radial intracellular potential, the bidomain equations governing electrical propagation in the conduction system are reduced to one dimension and coupled to a three-dimensional description of the myocardium. The interaction of the intracellular potential in the fiber with the surrounding extracellular potential is retained. To complete the model, and allow its use in simulations of the ventricles, a law governing current conservation at the specialized conduction system branch points and a model of current flow across discrete Purkinje-ventricular PV junctions are introduced. Numerical methods suitable for numerically approximating solutions to the model are introduced. By deriving such a bidomain model, combined with appropriate numerical methods, it is possible to model the electrical activity in the specialized conduction system of the ventricles in a detailed geometric model. The one-dimensional bidomain approach can be used to investigate regional and temporal variation in electrical activation of the heart, both under normal sinus rhythm and in the presence of large externally applied shocks.

2. Model development.

2.1. Three-dimensional fiber geometry. We now consider a domain $\Omega \in \mathbb{R}^3$ and introduce the three-dimensional region occupied by the fiber. The domains are shown in Figure 2.1(a) and can be defined as follows:

1. A one-dimensional manifold that will represent the idealized reduced fiber is denoted as Λ and defined by

$$(2.1) \qquad \Lambda = \{ \mathbf{x} \in \Omega \,|\, \mathbf{x} = \mathbf{x}_f(s), s \in (s_1, s_2) \},$$

where s is the curvilinear abscissa and $\mathbf{x}_f : (s_1, s_2) \to \mathbb{R}^3$ is a smooth map onto the fiber.

2. The fiber radius is given by a positive constant $R > 0$. This allows us to define the true fiber domain, Ω_f^R, as the set of points closer to Λ than R, such that

$$(2.2) \qquad \Omega_f^R = \{ \mathbf{x} \in \mathbb{R}^3 \,|\, dist(\mathbf{x}, \Lambda) < R \},$$

where $dist$ is the shortest distance from the point to the fiber. The fiber domain is assumed to be made up of myocardial tissue (mostly specialized conduction system myocytes and extracellular matrix), the electrophysiological properties of which can be modelled by the bidomain equations.

3. The area surrounding the fiber, Ω_b^R, is given by

$$(2.3) \qquad \Omega_b^R = \Omega \backslash \overline{\Omega_f^R}.$$

The surrounding region is assumed to be much larger than the fiber and is assumed to be a volume conductor. A volume conductor is a tissue or material that is capable of
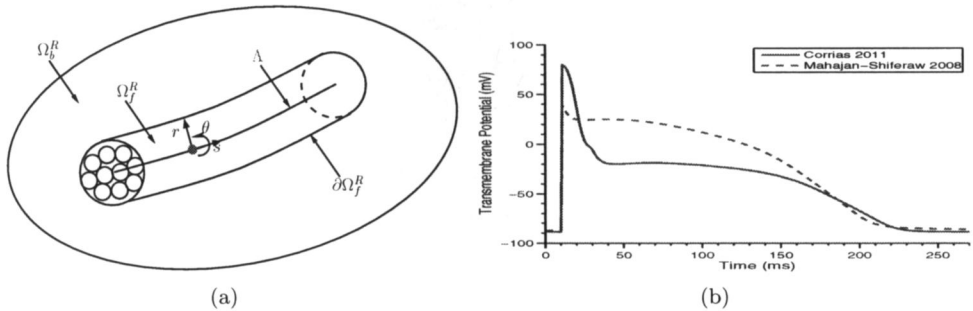
(a)   (b)

FIG. 2.1. (a) *A schematic of the domains used in the derivation of the one-dimensional fiber model. The center line of the fiber is Λ, which will represent the reduced fiber. The actual fiber domain Ω_f^R is assumed to be a tube of radius R around the center line. The fiber is made up of myocardial cells aligned along the fiber. The surrounding domain Ω is assumed to be much bigger than the fiber and to be a volume conductor. In the heart it will be made up of blood, a perfusing bath, or myocardial tissue. The interface between the fiber domain and the volume conductor is denoted by $\partial\Omega_f^R$.* (b) *Comparison of the action potentials generated by a specialized conduction system myocyte ionic model (Corrias model)* [9] *and a ventricular myocyte ionic model (Mahajan–Shiferaw model)* [23]. *The Corrias model is seen to have a faster upstroke velocity, lower plateau potential, and slightly longer action potential duration than the Mahajan–Shiferaw model.*

transmitting an electric or magnetic field. Cardiac tissue, blood, and perfusing baths used in cardiac electrophysiology experiments are all examples of volume conductors. For the purpose of deriving our model we assume that Ω_b^R is a passive volume conductor, such as blood or a perfusing bath. The extension to Ω_b^R being made up of myocardial tissue, as is the case for endocardial bound Purkinje fibers, is considered in section 2.6.

4. The interface between the fiber and the volume conductor is denoted $\partial\Omega_f^R$. Specialized conduction system fibers are known to have a collagen sheath that isolates them from the surrounding tissue. This collagen sheath is not explicitly represented in the model.

2.2. Specialized conduction system fiber equations. A number of fundamental assumptions about electrical propagation in myocardial tissue are used when deriving the governing equations for the model presented here. Specialized conduction system fibers consist of a bundle of cells arranged into a fiber. As such, fibers may not be accurately modelled as a unicellular excitable fiber such as a nerve dendrite or single striated muscle strand [33]. Instead, fibers may be modelled as a three-dimensional bidomain model [25].

In an homogenized sense, the relationship between current and potential in the two phases of the bidomain model is considered to be ohmic, such that

$$\text{(2.4a)} \qquad\qquad J_i = -\sigma_i \nabla \phi_i,$$
$$\text{(2.4b)} \qquad\qquad J_e = -\sigma_e \nabla \phi_e,$$

where J_i and J_e are current densities in the intra- and extracellular spaces, respectively; σ_i and σ_e are conductivity tensors, defined during the homogenization process and dependent on the prevailing myocyte fiber directions; ϕ_i and ϕ_e are the intracellular and extracellular potentials. Considering a small patch of isopotential membrane and conservation of current, the gradient of the current densities can be directly related to the current across the cellular membrane, known as the transmembrane

current, such that

$$(2.5a) \qquad \beta i_m = \nabla \cdot (\sigma_i \nabla \phi_i),$$

$$(2.5b) \qquad \beta i_m = -\nabla \cdot (\sigma_e \nabla \phi_e),$$

where β is the surface area to volume ratio of the myocytes. i_m is the total transmembrane current, such that

$$(2.6) \qquad i_m = C_m \frac{\partial v}{\partial t} + i_{ion}(v, \mathbf{u}),$$

where C_m is the capacitance of the cellular membrane, $v = \phi_i - \phi_e$ is the transmembrane potential, i_{ion} is a nonlinear function representing the ionic currents, and $\mathbf{u}$ is a vector of state variables for an electrophysiology cell model. The dynamics of the electrophysiology cell model are governed by a set of nonlinear ordinary differential equations, such that

$$(2.7) \qquad \frac{\partial \mathbf{u}}{\partial t} = \mathbf{f}(v, \mathbf{u}).$$

A significant number of electrophysiology cell models have been developed that can be used with the bidomain equations. Cell models range from simple phenomenological models, such as the Fitzhugh–Nagumo model [14], to detailed biophysical models that describe the major ionic currents found in cardiac myocytes, such as those used in this paper. Cell models are typically developed to represent the dynamics of myocytes in a specific species and tissue type in the heart. As such, the choice of cell model(s) for use with the bidomain equations is a complicated one that depends on the application for which the bidomain equations are being used.

Action potentials produced by Purkinje myocytes, as found in the specialized conduction system, feature a faster upstroke, longer duration, and lower (negative) plateau potential than those produced by ventricular myocytes. In this paper, we use two recent rabbit-specific biophysically detailed models to represent specialized conduction system and ventricular myocyte membrane kinetics. The Corrias model [9] is used to represent membrane kinetics in the specialized conduction system, and the Mahajan–Shiferaw model [23] is used for ventricular tissue. Figure 2.1(b) compares the action potentials generated by the Corrias and Mahajan–Shiferaw models.

Thus, the bidomain equations for a single fiber surrounded by a passive volume conductor, as shown in Figure 2.1(b), are given by

$$(2.8a) \qquad \beta i_m = \nabla \cdot (\sigma_i \nabla \phi_i) \qquad \text{in } \Omega_f^R,$$

$$(2.8b) \qquad \beta i_m = -\nabla \cdot (\sigma_e \nabla \phi_e) \qquad \text{in } \Omega_f^R,$$

$$(2.8c) \qquad \nabla \cdot (\sigma_b \nabla \phi_b) = 0 \qquad \text{in } \Omega_b^R,$$

where ϕ_b is the potential in the volume conductor and σ_b is the conductivity of the volume conductor. Boundary conditions are applied at the interface of the fiber with the volume conductor and at the edge of the volume conductor domain. The interface between the fiber and the surrounding domain, $\partial\Omega_f^R$, has boundary conditions

$$(2.9a) \qquad \mathbf{n} \cdot (\sigma_i \nabla \phi_i) = 0 \qquad \text{on } \partial\Omega_f^R,$$

$$(2.9b) \qquad \mathbf{n} \cdot (\sigma_e \nabla \phi_e) = \mathbf{n} \cdot (\sigma_b \nabla \phi_b) \qquad \text{on } \partial\Omega_f^R,$$

$$(2.9c) \qquad \phi_e = \phi_b \qquad \text{on } \partial\Omega_f^R,$$

where $\mathbf{n}$ is the outward facing normal of the fiber surface. Equation (2.9a) represents zero intracellular current flux, such that the intracellular space is insulated from the surrounding volume conductor. Equation (2.9b) represents continuity of potential in the extracellular space and the surrounding space. Equation (2.9c) specifies that all outside current entering the fiber flows into the extracellular space. At the edge of the volume conductor zero flux boundary conditions are imposed, such that

$$\mathbf{n} \cdot (\sigma_b \nabla \phi_b) = 0 \quad \text{on } \partial\Omega.$$

The zero flux boundary condition is chosen for clarity and is not restrictive on the derivation of the one-dimensional bidomain model.

With suitable assumptions on the regularity of ϕ_e and ϕ_b, (2.8b) and (2.8c) with transmission boundary conditions (2.9b) and (2.9c) may be rewritten as a single equation with discontinuous right-hand side and discontinuous conductivity tensor [28]. Thus, the bidomain representation of the fiber becomes

(2.10a) $$\nabla \cdot (\sigma_i \nabla \phi_i) = \beta i_m \quad \text{in } \Omega_f^R,$$

(2.10b) $$\nabla \cdot (\sigma_e \nabla \phi_e) = \begin{cases} -\beta i_m & \text{in } \Omega_f^R, \\ 0 & \text{in } \Omega_b^R. \end{cases}$$

In this form, ϕ_e is both the extracellular potential in the fiber and the potential in the volume conductor.

The above system of equations is reduced to a one-dimensional model in two stages: the three-dimensional description of the intracellular current in the fiber (2.10a) is reduced to one dependent only on the axial space variable by averaging over the fiber cross section. Subsequently, the radius of the fiber is reduced to zero by the use of an expansion in the radial variable.

2.2.1. Radially averaged intracellular equation. The following equations use a cylindrical coordinate system (r, θ, s) with the s-axis aligned with the local fiber axial direction. Several assumptions are made to allow the reduction of (2.10a) to a one-dimensional model:

(A1) The Purkinje myocyte cells are aligned along the fiber and are evenly distributed perpendicular to the fiber. The alignment is such that the intracellular conductivity tensor is diagonal in local cylindrical coordinates. Thus, in local cylindrical coordinates,

(2.11) $$\sigma_i \nabla_\theta v = \left(\sigma_i^r \frac{\partial v}{\partial r}, \sigma_i^\theta \frac{1}{r} \frac{\partial v}{\partial \theta}, \sigma_i^s \frac{\partial v}{\partial s} \right)^T,$$

where ∇_θ is the gradient operator in cylindrical coordinates and σ_i^r, σ_i^θ, and σ_i^s are constant.

(A2) The radial length scale is much smaller than the axial one, such that

$$\frac{R_0}{L_0} \ll 1,$$

where R_0 is the typical radius and L_0 is the typical length of a fiber.

(A3) Fiber radius is constant in time and space, i.e., $\frac{\partial R}{\partial t} = 0$ and $\frac{\partial R}{\partial s} = 0$. The averaging operator on the cross section of a fiber of radius R, perpendicular to the line Λ, is denoted by a bar:

(2.12) $$\bar{g}(s) = \frac{1}{\pi R^2} \int_0^R \int_0^{2\pi} g(s, r, \theta) r \, dr d\theta.$$

In cylindrical coordinates, subject to assumption (A1), the intracellular equation (2.10a) becomes

$$(2.13) \qquad \beta i_m = \sigma_i^r \frac{1}{r} \frac{\partial}{\partial r} \left(r \frac{\partial \phi_i}{\partial r} \right) + \sigma_i^\theta \frac{1}{r^2} \frac{\partial^2 \phi_i}{\partial \theta^2} + \sigma_i^s \frac{\partial^2 \phi_i}{\partial s^2}.$$

We integrate over the fiber's cross section to obtain the averaged equations. Integrating (2.13) from $r = 0$ to $r = R$ and $\theta = 0$ to $\theta = 2\pi$ gives

$$(2.14) \quad \beta \int_0^R \int_0^{2\pi} i_m r \, \mathrm{d}\theta \mathrm{d}r = \int_0^R \int_0^{2\pi} \sigma_i^r \frac{\partial}{\partial r} \left(r \frac{\partial \phi_i}{\partial r} \right) + \sigma_i^\theta \frac{1}{r} \frac{\partial^2 \phi_i}{\partial \theta^2} \, \mathrm{d}\theta \mathrm{d}r$$
$$+ \sigma_i^s \int_0^R \int_0^{2\pi} \frac{\partial^2 \phi_i}{\partial s^2} r \, \mathrm{d}\theta \mathrm{d}r.$$

The two terms of the integrand of the first integral on the right-hand side of (2.14) are a two-dimensional Laplacian in polar coordinates. Applying the divergence theorem to the cross-sectional disk and boundary condition (2.9a) yields that this term is zero. The averaged equation is

$$\beta \int_0^R \int_0^{2\pi} i_m r \, \mathrm{d}\theta \mathrm{d}r = \sigma_i^s \int_0^R \int_0^{2\pi} \frac{\partial^2 \phi_i}{\partial s^2} r \, \mathrm{d}\theta \mathrm{d}r.$$

Leibniz' theorem is applied repeatedly, noting that $\frac{\partial R}{\partial s} = 0$ and $\frac{\partial R}{\partial t} = 0$, to give

$$\beta \overline{i_m} = \beta \left(C_m \frac{\partial \overline{v}}{\partial t} + \overline{i_{ion}}(v, \mathbf{u}) \right) = \sigma_i^s \frac{\partial^2 \overline{\phi_i}}{\partial s^2}.$$

Rewriting in terms of ϕ_i and ϕ_e gives

$$(2.15) \qquad \beta i_m = \beta \left(C_m \frac{\partial(\overline{\phi_i} - \overline{\phi_e})}{\partial t} + i_{ion}(\overline{\phi_i} - \overline{\phi_e}, \mathbf{u}) \right) = \sigma_i^s \frac{\partial^2 \overline{\phi_i}}{\partial s^2}.$$

The equation governing the intracellular current has been reduced to one dependent only on the axial space variable. Equation (2.15) is expressed in terms of the averaged quantities $\overline{\phi_i}$ and $\overline{\phi_e}$. The averaged intracellular potential $\overline{\phi_i}$ can be used directly while solving (2.15), and there is no need to solve for ϕ_i. The ionic current term, i_{ion}, is a nonlinear function of v, and its averaged value will have to be calculated numerically. To simplify the exposition, the bar notation for $\overline{\phi_i}$ and $\overline{i_{ion}}$ is dropped in subsequent sections. Equation (2.15) depends on the cross-sectional average of the extracellular potential, $\overline{\phi_e}$, which must be obtained from the three-dimensional representation of the surrounding volume conductor. These issues will be discussed in section 2.3.1.

2.2.2. The one-dimensional extracellular equation. The preceding derivation reduces the intracellular equation (2.10a) to one that is dependent only on the axial space variable. However, the extracellular equation (2.10b) still requires a three-dimensional representation of the fiber in the domain Ω. This requirement is now removed by reducing the three-dimensional fiber to an idealized one-dimensional manifold. The reduction proceeds in weak form, as this allows the domain of the fiber to be more easily manipulated, but at the cost of imposing a smoothness requirement on the solutions. A derivation using the strong form of the equations would be preferable, but we do not attempt this here.

From the previous section, the averaged equations governing propagation on the Purkinje fiber are given by

$$(2.16a) \qquad \beta i_m = \sigma_i^s \frac{\partial^2}{\partial s^2}(v + \overline{\phi_e}) \quad \text{in } \Lambda,$$

$$(2.16b) \qquad \nabla \cdot (\sigma_e \nabla \phi_e) = \begin{cases} -\beta i_m & \text{in } \Omega_f^R, \\ 0 & \text{in } \Omega_b^R. \end{cases}$$

Equation (2.16b) is multiplied by an arbitrary test function $\psi \in C^\infty(\overline{\Omega})$ and integrated over Ω to give

$$(2.17) \qquad \begin{aligned} \int_\Omega \sigma_e \nabla \phi_e \cdot \nabla \psi \, \mathrm{d}\Omega &= \int_{\Omega_b^R} \sigma_e \nabla \phi_e \cdot \nabla \psi \, \mathrm{d}\Omega + \int_{\Omega_f^R} \sigma_e \nabla \phi_e \cdot \nabla \psi \, \mathrm{d}\Omega \\ &= \beta \int_{\Omega_f^R} i_m \psi \, \mathrm{d}\Omega. \end{aligned}$$

Putting the right-hand side of (2.17) into cylindrical coordinates and rewriting in terms of the averaged transmembrane current gives

$$(2.18) \qquad \int_\Omega \sigma_e \nabla \phi_e \cdot \nabla \psi \, \mathrm{d}\Omega = \beta \int_{s_1}^{s_2} \overline{i_m} \int_0^{2\pi} \int_0^R \psi r \, \mathrm{d}r\mathrm{d}\theta\mathrm{d}s.$$

As before, we drop the bar notation on the averaged transmembrane current to simplify the exposition. Assumption (A2), that the radius of the fiber is assumed to be much smaller than the length of Λ, is used to evaluate the right-hand side of (2.18).

A Taylor series expansion for ψ about $r = 0$ is given by

$$(2.19) \qquad \psi(s, r, \theta) = \psi(s, 0, 0) + r\psi'(s, 0, \theta) + \frac{r^2}{2}\psi''(s, 0, \theta) + \cdots.$$

Inserting (2.19) into (2.18) and integrating about the axis with respect to r, from 0 to R, gives

$$\begin{aligned} \int_\Omega &\sigma_e \nabla \phi_e \cdot \nabla \psi \, \mathrm{d}\Omega \\ &= \beta \int_{s_1}^{s_2} i_m \int_0^{2\pi} \frac{R^2}{2}\psi(s, 0, 0) + \frac{R^3}{3}\psi'(s, 0, \theta) + \frac{R^4}{8}\psi''(s, 0, \theta) + \cdots + \mathrm{d}\theta\mathrm{d}s. \end{aligned}$$

Discarding terms of order R^3 and higher, then integrating the remaining constant with respect to θ, gives

$$(2.20) \qquad \int_\Omega \sigma_e \nabla \phi_e \cdot \nabla \psi \, \mathrm{d}\Omega = \beta \pi R^2 \int_{s_1}^{s_2} i_m \psi_0 \mathrm{d}s + O(R^3).$$

We note that the right-hand side of (2.20) is $O(R^2)$ and, in isolation, will have only a small influence on the extracellular potential. Such a small effect will not significantly alter conduction velocity in a fiber. However, we are interested in a network of specialized conduction system fibers embedded in the ventricles. In this setting, many fibers are found in close proximity to one another. The composite effect of several fibers on the extracellular space is enough to affect the potential in

the extracellular space and thus propagation in the fiber. This is demonstrated in section 2.4.

Dropping terms of $O(R^3)$, (2.20) may be rewritten as

$$\int_\Omega \sigma_e \nabla \phi_e \cdot \nabla \psi \, \mathrm{d}\Omega \approx \beta \pi R^2 \int_\Lambda i_m \psi \mathrm{d}s \qquad \forall \psi \in C_0^\infty(\overline{\Omega}).$$

Thus, the three-dimensional representation of the fiber in the extracellular equation has been reduced to a one-dimensional representation valid for small R.

In strong form, the final reduced problem is the following: Find ϕ_i, ϕ_e, and $\mathbf{u}$, such that

$$(2.21a) \qquad \beta \left(C_m \left(\frac{\partial \phi_i}{\partial t} - \frac{\partial \overline{\phi_e}}{\partial t} \right) + i_{ion}(v, \mathbf{u}) \right) = \sigma_i^s \frac{\partial^2 \phi_i}{\partial s^2} \qquad \text{in } \Lambda,$$

$$(2.21b) \qquad -\beta \pi R^2 \left(C_m \left(\frac{\partial \phi_i}{\partial t} - \frac{\partial \overline{\phi_e}}{\partial t} \right) + i_{ion}(v, \mathbf{u}) \right) \delta_\Lambda = \nabla \cdot (\sigma_e \nabla \phi_e) \qquad \text{in } \Omega,$$

$$(2.21c) \qquad \frac{\partial \mathbf{u}}{\partial t} = \mathbf{f}(v, \mathbf{u}) \qquad \text{in } \Lambda,$$

$$(2.21d) \qquad \frac{\partial \phi_e}{\partial \mathbf{n}} = 0 \qquad \text{on } \partial\Omega,$$

where $v = \phi_i - \overline{\phi_e}$ and δ_Λ is defined as a Dirac measure on Λ, such that for $g \in L^2(\Lambda)$,

$$\int_\Omega g \delta_\Lambda \, \mathrm{d}\Omega = \int_\Lambda g \, \mathrm{d}s.$$

2.3. Weak formulation. Equations (2.21a) and (2.21b) form a one-dimensional problem for a single specialized conduction system fiber embedded in a passive three-dimensional volume conductor. The reduced model has introduced a measure term and an averaging operator into the system of equations. The presence of the measure term and averaging operator in (2.21a) and (2.21b) significantly complicate the model and the numerical techniques required to approximate solutions to it. In particular, the measure term δ_Λ is known not to be in the dual space of H^1, and therefore standard existence and uniqueness results based on this space do not hold for this problem [34]. D'Angelo and Quarteroni [12] proved existence and uniqueness for non–time-dependent equations of this type to study blood flow in tissue perfusion problems. Their analysis is based on the weighted space

$$H_\alpha^1(\Omega) = \{u \in L_\alpha^2(\Omega) : \nabla u \in (L_\alpha^2(\Omega))^3\},$$

where $\alpha \in (-1, 1)$ and $L_\alpha^2(\Omega)$ is the space of measurable functions, u, such that

$$\int_\Omega u^2 d^{2\alpha} \, \mathrm{d}x < \infty,$$

where d is the distance from the idealized fiber, Λ. The same weighted space will be used to study the model presented here.

In weak form, (2.21a) and (2.21b) are as follows: Find $\phi_e \in H_\alpha^1(\Omega)$ and $\phi_i \in H^1(\Lambda)$, such that

$$(2.22) \qquad \beta \int_\Lambda C_m \left(\frac{\partial \phi_i}{\partial t} - \frac{\partial \overline{\phi_e}}{\partial t} \right) \psi_i + i_{ion}(v, \mathbf{u}) \psi_i \, ds + \int_\Lambda \sigma_i^s \frac{\partial \phi_i}{\partial s} \frac{\partial \psi_i}{\partial s} \, ds = 0,$$

$$(2.23) \quad -\beta \pi R^2 \int_\Lambda C_m \left(\frac{\partial \phi_i}{\partial t} - \frac{\partial \overline{\phi_e}}{\partial t} \right) \psi_e + i_{ion}(v, \mathbf{u}) \psi_e \, ds + \int_\Omega \sigma_e \nabla \phi_e \cdot \nabla \psi_e \, d\Omega = 0$$

for all $\psi_e \in H_{-\alpha}^1(\Omega)$ and $\psi_i \in H^1(\Lambda)$.

A semi-implicit discretization in time is applied to the reduced equations [18, 44]. This discretization uses a backward Euler approximation for the spatial derivatives and a forward approximation for the nonlinear reaction terms. The discretization allows the intracellular and extracellular potentials to be calculated using a single linear solve. The equations that govern the remainder of the dependent variables of the model then uncouple into a small system of ordinary differential equations at each point in Λ. Discretizing in time, we have

$$(2.24) \quad \kappa \int_\Lambda (\phi_i^n - \overline{\phi_e}^n) \psi_i \, ds + \int_\Lambda \sigma_i^s \frac{\partial \phi_i^n}{\partial s} \frac{\partial \psi_i}{\partial s} \, ds$$
$$= \kappa \int_\Lambda (\phi_i^{n-1} - \overline{\phi_e}^{n-1}) \psi_i \, ds - \beta \int_\Lambda i_{ion}(v^n, \mathbf{u}^{n-1}) \psi_i \, ds,$$

$$(2.25) \quad \kappa \int_\Lambda (\overline{\phi_e}^n - \phi_i^n) \psi_e \, ds + \frac{1}{\pi R^2} \int_\Omega \sigma_e \nabla \phi_e^n \cdot \nabla \psi_e \, d\Omega$$
$$= \kappa \int_\Lambda (\overline{\phi_e}^{n-1} - \phi_i^{n-1}) \psi_e \, ds + \beta \int_\Lambda i_{ion}(v^{n-1}, \mathbf{u}^{n-1}) \psi_e \, ds,$$

$$(2.26) \qquad\qquad \mathbf{u}^n - \Delta t \mathbf{f}(v^{n-1}, \mathbf{u}^n) = \mathbf{u}^{n-1}$$

for all $\psi_e \in H_\alpha^1(\Omega)$ and $\psi_i \in H^1(\Lambda)$. Here superscript n indicates the discrete time-level, $\kappa = \frac{\beta C_m}{\Delta t}$, and Δt is the discrete time-step.

Thus, at each discrete time-level, the following problem is solved: Find $(\phi_e^n, \phi_i^n) \in H_\alpha^1(\Omega) \times H^1(\Lambda)$, such that

$$(2.27) \qquad a((\phi_e^n, \phi_i^n), (\psi_e, \psi_i)) = F(\psi_e, \psi_i) \qquad \forall (\psi_e, \psi_i) \in H_{-\alpha}^1(\Omega) \times H^1(\Lambda),$$

where

(2.28)
$$a(\boldsymbol{\phi}^n, \boldsymbol{\psi}) = \kappa \int_\Lambda (\phi_i^n - \overline{\phi_e}^n)(\psi_i - \psi_e) ds + \frac{1}{\pi R^2} \int_\Omega \sigma_e \nabla \phi_e^n \cdot \nabla \psi_e d\Omega + \int_\Lambda \sigma_i^s \frac{\partial \phi_i^n}{\partial s} \frac{\partial \psi_i}{\partial s} ds,$$

(2.29)
$$F(\boldsymbol{\psi}) = \kappa \int_\Lambda (\phi_i^{n-1} - \overline{\phi_e}^{n-1})(\psi_i - \psi_e) ds + \beta \int_\Lambda i_{ion}(v^{n-1}, u^{n-1})(\psi_e - \psi_i) ds.$$

In the appendix, we show that a solution exists and is unique at each time-step for the time-discrete equations (2.27).

2.3.1. Numerical approximation. Following the approach of [11], a finite element approximation to (2.27) can be made by replacing the spaces $H_\alpha^1(\Omega)$ and $H^1(\Lambda)$ with discrete spaces spanned by suitable first order Lagrangian finite element basis functions. It is assumed that the domain Ω is the union of tetrahedral elements, $\mathcal{T}_h$. The fiber domain, Λ, is discretized by extracting edges from the three-dimensional mesh discretization of Ω. The disadvantage of this approach is that it removes smoothness of the domain Λ. However, the use of an extracted domain significantly simplifies the finite element implementation. The fiber domain is a collection $\mathcal{I}_h$ of edges I_k of tetrahedra in $\mathcal{T}_h$, such that

$$(2.30) \qquad \Lambda = \bigcup_{I_k \in \mathcal{I}_h} I_k.$$

Thus, the nodes in the one-dimensional mesh are a subset of the nodes in the three-dimensional mesh. We denote by $\mathbf{x}_i^k, k = 1, \ldots, N_{i,h}$, the one-dimensional nodes and by $\mathbf{x}_e^l, l = 1, \ldots, N_{e,h}$ the three-dimensional nodes.

Lagrangian basis functions for the three-dimensional domain are denoted by $\{\psi_{e,k}\}, k = 1, \ldots, N_{e,h}$. Lagrangian basis functions for the one-dimensional domain are denoted by $\{\psi_{i,k}\}, k = 1, \ldots, N_{i,h}$ and are assumed to be the restriction of the three-dimensional basis functions onto Λ. A function, denoted by $r_\Lambda : k \to l$, is defined that maps each one-dimensional node index to the corresponding three-dimensional one:

$$(2.31) \qquad \forall k \in (1, \ldots, N_{i,h}) : \qquad \mathbf{x}_e^{r_\Lambda(k)} = \mathbf{x}_i^k \quad \text{and} \quad \psi_{i,k} = \psi_{e,r_\Lambda(k)} \text{ on } \Lambda.$$

Using r_Λ we define the extension matrix R_Λ, such that

$$(2.32) \qquad (R_\Lambda)_{kl} = \begin{cases} 1 & \text{if } k = r_\Lambda(l), \\ 0 & \text{otherwise.} \end{cases}$$

For suitable basis functions, (2.27) becomes a linear system of equations that can be expressed in matrix form. Let $\boldsymbol{\phi}_e = (\phi_{e,h}^1, \ldots, \phi_{e,h}^{N_{e,h}})$ and $\boldsymbol{\phi}_i = (\phi_{i,h}^1, \ldots, \phi_{i,h}^{N_{i,h}})$ be the coefficients of the approximate solution. Then, in matrix form, the finite element problem reads as

$$(2.33) \quad \begin{bmatrix} \frac{1}{\pi R^2} K + \kappa R_\Lambda \overline{M} & -\kappa R_\Lambda \hat{M} \\ -\kappa \overline{M} & \hat{K} + \kappa \hat{M} \end{bmatrix} \begin{bmatrix} \boldsymbol{\phi}_e^n \\ \boldsymbol{\phi}_i^n \end{bmatrix}$$

$$= \begin{bmatrix} \kappa R_\Lambda \overline{M} & -\kappa R_\Lambda \hat{M} \\ -\kappa \overline{M} & \kappa \hat{M} \end{bmatrix} \begin{bmatrix} \boldsymbol{\phi}_e^{n-1} \\ \boldsymbol{\phi}_i^{n-1} \end{bmatrix} + \begin{bmatrix} \beta R_\Lambda \hat{M} \boldsymbol{I}_{ion}(\boldsymbol{v}^{n-1}, \mathbf{u}^{n-1}) \\ -\beta \hat{M} \boldsymbol{I}_{ion}(\boldsymbol{v}^{n-1}, \mathbf{u}^{n-1}) \end{bmatrix},$$

where the blocks of the matrix are given by

$$(2.34a) \qquad K_{kl} = \int_\Omega \sigma_e \nabla \psi_{e,k} \cdot \nabla \psi_{e,l} \, d\Omega, \qquad k, l = 1, \ldots, N_{e,h},$$

$$(2.34b) \qquad \hat{K}_{kl} = \int_\Lambda \sigma_i^s \frac{\partial \psi_{i,k}}{\partial s} \frac{\partial \psi_{i,l}}{\partial s} \, ds, \qquad k, l = 1, \ldots, N_{i,h}$$

and

$$(2.35a) \qquad \hat{M}_{kl} = \int_\Lambda \psi_{i,k} \psi_{i,l} \, ds, \qquad k, l = 1, \ldots, N_{i,h},$$

$$(2.35b) \qquad \overline{M}_{kl} = \int_\Lambda \psi_{i,k} \overline{\psi_{i,l}} \, ds, \qquad k, l = 1, \ldots, N_{i,h}.$$

The block matrices in (2.33) consist of stiffness and mass matrices calculated on the three-dimensional and one-dimensional meshes, and a matrix $\overline{M}$ that contains the averaging operator (2.12). The elements of this matrix are given by
(2.36)

$$\overline{M}_{kl} = \int_\Lambda \psi_{i,k}\overline{\psi_{e,l}}\,\mathrm{d}s = \sum_{I_m \in \mathcal{I}_m} \int_{I_m} \psi_{i,k}(s) \left(\frac{1}{\pi R^2} \int_0^R \int_0^{2\pi} \psi_{e,l}(s,r,\theta)\mathrm{d}\theta\mathrm{d}r \right) \mathrm{d}s.$$

Here, the averaging operator is embedded within the terms of the matrix and must be calculated as a part of the assembly process. This will have to be done using numerical integration and will, in general, require the value of the basis functions at points lying within the disk described in local coordinates by (s, R, θ) for $r \in [0, R]$ and $\theta \in [0, 2\pi]$.

To approximate the integral on I_m in (2.36), we use a quadrature formula on the reference interval $[0, 1]$, with nodes s_m and weights ω_m, with $m = 1, \ldots, N_m$. To approximate the integrals over θ and r, a second quadrature formula on the reference unit disk is used, with node points (r_n, θ_n) and weights ω_n, with $n = 1, \ldots, N_n$. Using these quadrature rules, we can write

$$(2.37) \quad \int_{I_m} \psi_{i,k}(s) \left(\frac{1}{\pi R^2} \int_0^R \int_0^{2\pi} \psi_{e,l}(s,r,\theta)\mathrm{d}\theta dr \right) \mathrm{d}s$$

$$\approx \sum_{m=1}^{N_m} \psi_{i,k}(s_m) \left(\sum_{n=1}^{N_n} \psi_{e,l}(s_m, r_n, \theta_n)\omega_n \right) J_m\omega_m,$$

where J_m is the Jacobian of the transformation to the reference interval at s_m. To apply an integration formula like this, it is necessary to calculate the value of $\psi_{e,l}$ at the quadrature points (s_m, r_n, θ_n). This requires finding the tetrahedral element containing the point and computing the corresponding values of the basis functions. Determining the enclosing tetrahedra of arbitrary points is a computationally expensive procedure, even for a relatively small number of quadrature points. The resulting system matrix is also nonsymmetric, limiting the choice of linear solvers. Thus, it is necessary to investigate how this cost can be minimized or avoided. The trade-off between accuracy and computational efficiency using a one-dimensional model embedded in a three-dimensional model is investigated extensively in [11], with the conclusion that a lumped approximation to the problem may be used under certain assumptions. If R is smaller than the typical tetrahedra size, h, as would be expected in the situation where this reduction would be useful, the lumped approximation $\overline{\phi}_e \approx \phi_e(s, 0, 0)$ may be used. The lumped approximation is equivalent to

$$\overline{M} \approx \hat{M}R_\Lambda^T,$$

which can be directly substituted in (2.33). Using the lumped approximation, it is straightforward to show that the system matrix in (2.33) is symmetric and positive definite.

2.3.2. Convergence test. To test the numerical method, a convergence test is performed on a simplified problem with a known analytical solution. The convergence test is adapted from one in [11] for use with the cross section averaging operator (2.12). Consider a single specialized conduction system fiber, of radius R, running along the axis of a cylinder of radius 1 and height 1, as shown in Figure 2.5(a). A fiber at steady

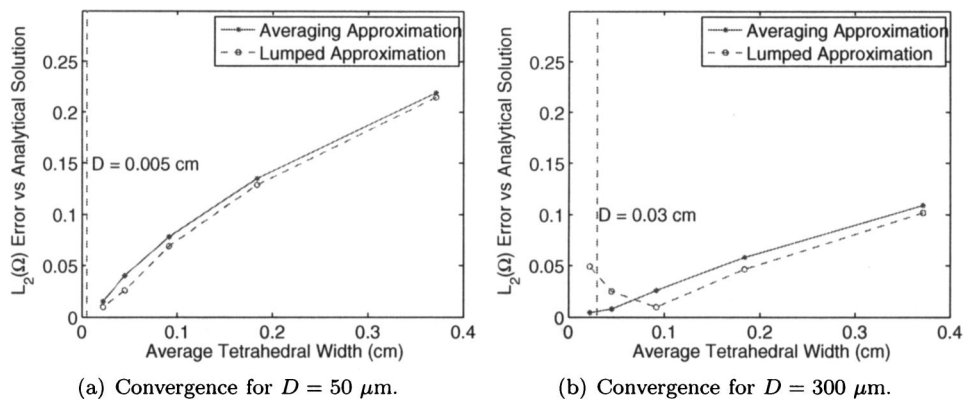(a) Convergence for $D = 50\ \mu$m.   (b) Convergence for $D = 300\ \mu$m.

FIG. 2.2. *Convergence in the $L_2(\Omega)$ norm of the lumped and averaging approximation schemes for the convergence test problem (2.38a)–(2.39e). The vertical dashed lines indicate the radius of the fiber. The averaging approximation (solid lines) converges fully. The lumped approximation (curved dashed lines) converges initially, but convergence ceases as the average tetrahedral width approaches the fiber diameter.*

state with a simple linear ionic cell model can be modelled by

$$(2.38a) \qquad -\nabla \cdot (\sigma_e \nabla \phi_e) + \beta(\overline{\phi_e} - \phi_i)\delta_\Lambda = 0 \qquad \text{in } \Omega,$$

$$(2.38b) \qquad -\frac{\partial}{\partial z}\left(\sigma_i \frac{\partial \phi_i}{\partial z}\right) + \beta(\phi_i - \overline{\phi_e}) = 0 \qquad \text{in } \Lambda,$$

with $\sigma_e = 1$, $\sigma_i(z) = 1 + z + \frac{1}{2}z^2$, and $\beta = \frac{4\pi}{2\log R - 1 + 4\pi}$. Subject to boundary conditions

$$(2.39a) \qquad \phi_e = 0 \qquad \text{for } r = 1,$$

$$(2.39b) \qquad \frac{\partial \phi_e}{\partial \mathbf{n}} = -\frac{1}{2\pi}\log r \qquad \text{for } z = 1,$$

$$(2.39c) \qquad \frac{\partial \phi_e}{\partial \mathbf{n}} = \frac{1}{2\pi}\log r \qquad \text{for } z = 0,$$

$$(2.39d) \qquad \phi_i = 1 \qquad \text{at } z = 0,$$

$$(2.39e) \qquad \phi_i = 2 \qquad \text{at } z = 1,$$

the problem can be shown to have solution

$$\phi_e(z, r, \theta) = -\frac{1+z}{2\pi}\log r,$$

$$\phi_i(z) = 1 + z.$$

In problem (2.38a)–(2.39e), all lengths are given in cm, potentials in mV, and conductivities in mS. The problem was solved on an unstructured tetrahedral mesh using the scheme described in section 2.3.1. A third order, four point, quadrature rule was used to approximate the averaging operator over the fiber cross section [20]. The spatial resolution of the mesh was increased repeatedly to assess convergence of the numerical approximation, both for the averaging approximation and for the lumped approximation. Figure 2.2 shows convergence of the averaging and lumped numerical schemes for a fiber of diameter 50 μm and a fiber of diameter 300 μm. Error norms were calculated using a 10th order Gaussian quadrature rule on each

(a) Averaging approximation $D = 50$ μm.

(b) Lumped approximation $D = 50$ μm.

(c) Averaging approximation $D = 300$ μm.

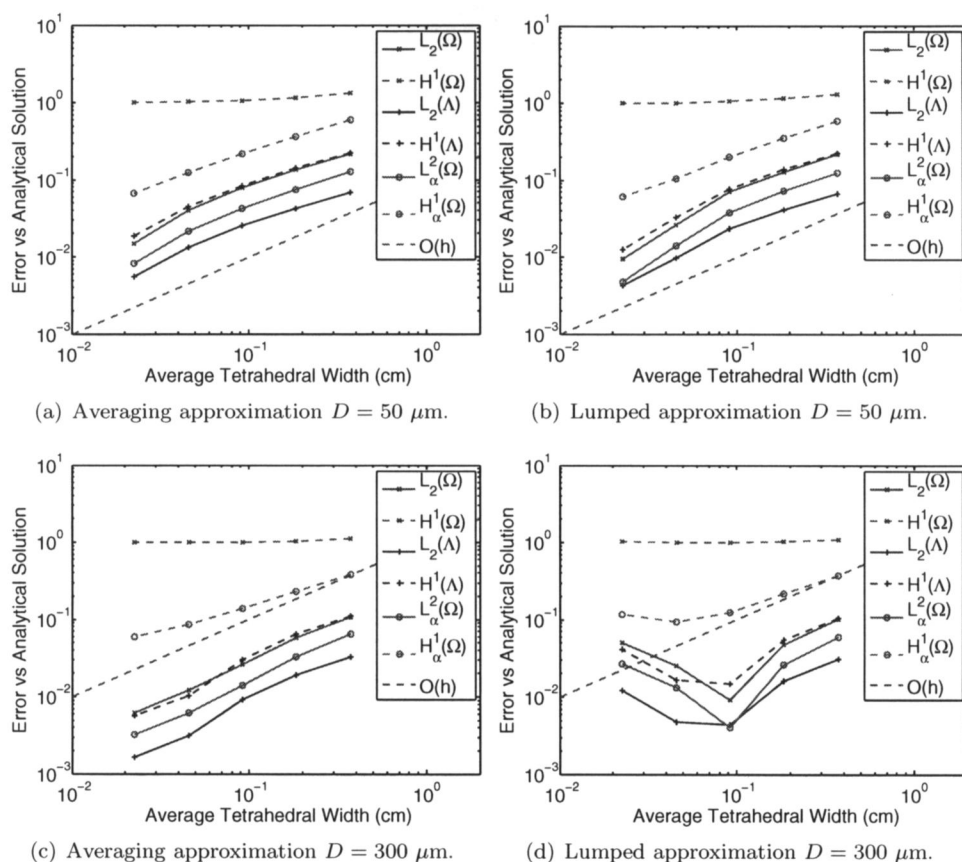(d) Lumped approximation $D = 300$ μm.

FIG. 2.3. *Convergence rates in different norms of the lumped and averaging approximation schemes for the convergence test problem* (2.38a)–(2.39e). (a) *and* (b) *show convergence rates for a fiber of diameter* 5 μm, *and* (c) *and* (d) *show convergence rates for a fiber of diameter* 300 μm. *The dashed line indicates* $O(h)$ *convergence to allow comparison of the convergence rates.*

element. The averaging approximation converges fully and the lumped approximation converges initially in both cases. Convergence of the lumped approximation stops as the average tetrahedral width approaches the fiber diameter, as expected. However, in ventricular simulations the average tetrahedral width is typically much larger than the fiber radius, and the lumped approximation is applicable.

To assess the rate of convergence of the scheme, Figure 2.3 shows log-log plots of the error in various norms against the average tetrahedral width. As expected from the discussion in section 2.3, in each case the scheme failed to converge for ϕ_e in the $H^1(\Omega)$ norm. Convergence for ϕ_e was recovered in the weighted $H^1_\alpha(\Omega)$ norm, where slightly better than $O(h^{\frac{1}{2}})$ convergence was observed. Order $O(h)$ convergence was observed for ϕ_e in the remaining norms and for ϕ_i in the $L_2(\Lambda)$ and $H^1(\Lambda)$ norms.

2.4. Influence of multiple fibers on activation threshold. During the derivation of the one-dimensional bidomain model we observed that the transmembrane current flowing from a single fiber into the extracellular domain could be too small to significantly affect propagation in the fiber. However, the specialized conduction system consists of a network of fibers in close proximity to one another, and

TABLE 2.1
The minimum shock and fields strengths required to excite propagation in a number of specialized conduction system fibers arranged in parallel.

| Number of fibers	Fiber diameter (μm)	Shock threshold (μ A/cm)	Field threshold (V/cm)
1	50	369	1.23
7	50	372	1.24
1	300	380	1.27
3	300	399	1.33
5	300	411	1.37

the influence of several fibers on the extracellular potential can be enough to alter propagation dynamics.

To demonstrate this, we set up a series of simulations in a 0.2cm × 0.2cm square domain. A specialized conduction system fiber of length 0.2cm was positioned in the center of the domain. The Corrias model [9] was used to represent membrane kinetics in the fiber. Intracellular conductivity in the specialized conduction system was set to 4 mS cm^{-1}, and the cell surface to volume ratio in the fiber was set to 2800 cm^{-1}. Electrodes were placed on either side of the domain and a strong extracellular field, whose gradient was aligned parallel to the fiber, was applied for 1 ms. The simulation was repeated with the extracellular field strength increased until the field excited propagation in the fiber. The number and diameter of the fibers were varied, with multiple fibers aligned parallel to each other, with their center lines twice their radius apart, so that they are touching. The simulations were repeated to assess the difference in threshold required to activate the fibers.

Table 2.1 shows the minimum shock strength required to activate the fibers in each case. We see a difference of 10% in minimum shock strength required to activate the different fiber configurations. This difference is produced by the current flowing between the fibers and the extracellular space during the application of the shock. This difference may be an important determinant in successful defibrillation of the specialized conduction system and justifies the inclusion of the $O(R^2)$ term in section 2.2.2.

2.5. Branching model. The equations governing conservation of intracellular current at fiber branch points are now introduced in order to model electrical activation through a branching structure such as the cardiac specialized conduction system. Previously published one-dimensional specialized conduction system models have imposed Kirchoff's current law at each branch point [2, 41]. However, imposing Kirchoff's law has previously been achieved by the use of a dedicated numerical technique, such as cubic Hermite basis functions [41] or the finite volume method [2], while the other equations are solved using the finite element method. The following scheme has been developed as a natural and computationally efficient extension to the linear finite element approximation presented in the previous section.

The branching model approximates the junction as a point joining three fibers. Figure 2.4(a) shows a schematic of a single branch point. The parent fiber entering the junction is denoted by Λ_1. The end of Λ_1 closest to the junction is denoted by B_1. Similarly, the two daughter fibers are labelled Λ_2 and Λ_3, with proximal ends of the fibers labelled A_2 and A_3, respectively. The radius of each fiber Λ_j is denoted by R_{Λ_j} and the intracellular conductivity of each fiber is labelled σ_{i_j}.
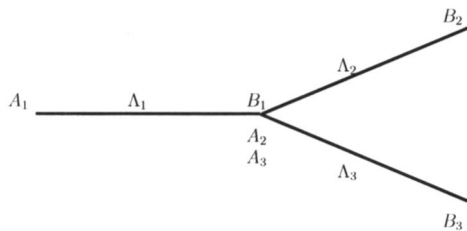
(a) The model branch point.
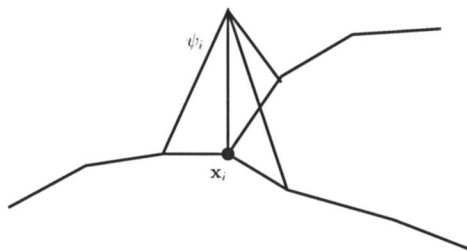
(b) A linear finite element basis function centered at the bifurcation.

FIG. 2.4. *A schematic diagram of a model branch point and depiction of a linear finite element basis function at a bifurcation.*
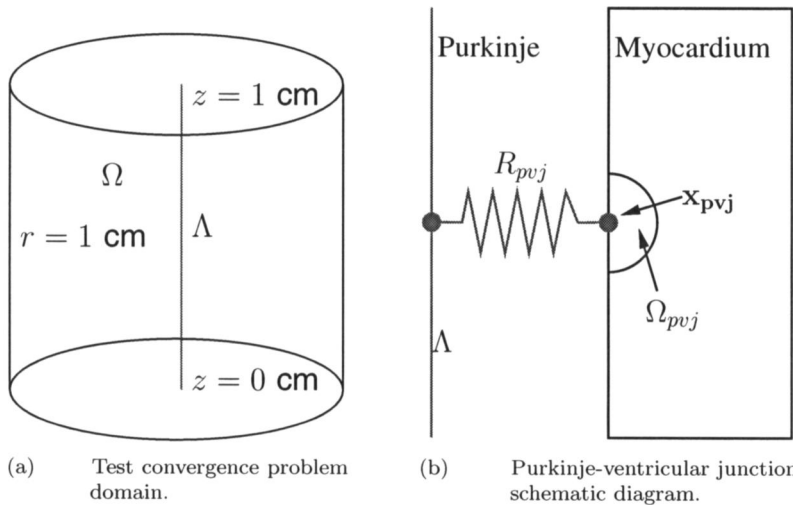

(a) Test convergence problem domain.

(b) Purkinje-ventricular junction schematic diagram.

FIG. 2.5. (a) *shows the domains used for the convergence test problem* (2.38a)–(2.39e). (b) *shows a schematic diagram of a PV junction. The Purkinje fiber domain,* Λ, *is connected to the myocardial domain,* Ω, *via a resistor at the point* $\mathbf{x_{pvj}}$. *The PV junction is linked to a hemispherical volumetric region in the myocardium, denoted by* Ω_{pvj}.

Conservation of current through the junction is governed by

$$(2.40) \qquad\qquad I_1 = I_2 + I_3,$$

where
(2.41)

$$I_1 = -\pi R_{\Lambda_1}^2 \sigma_{i_1} \left. \frac{\partial \phi_i}{\partial s} \right|_{B_1}, \quad I_2 = -\pi R_{\Lambda_2}^2 \sigma_{i_2} \left. \frac{\partial \phi_i}{\partial s} \right|_{A_2}, \quad I_3 = -\pi R_{\Lambda_3}^2 \sigma_{i_3} \left. \frac{\partial \phi_i}{\partial s} \right|_{A_3}.$$

We now show how these conditions can be enforced in the numerical solution scheme presented in the previous section.

2.5.1. Branch point model solution procedure. Consider (2.21a) for the model branch point domain. Following the standard procedure, the equations are put into weak form by multiplying (2.21a) by a suitable test function $\psi_i \in H^1(\Lambda)$ and integrating over Λ to give

$$\beta \int_{\Lambda_1 \cup \Lambda_2 \cup \Lambda_3} \left[C_m \left(\frac{\partial \phi_i}{\partial t} - \frac{\partial \overline{\phi}_e}{\partial t} \right) \psi_i + i_{ion}(v, \mathbf{u}) \psi_i \right] \mathrm{d}s = \int_{\Lambda_1 \cup \Lambda_2 \cup \Lambda_3} \sigma_i^s \frac{\partial^2 \phi_i}{\partial s^2} \psi_i \, \mathrm{d}s.$$

Each branch is considered separately, and integration by parts is applied to give

$$-\sigma_{i_1}^s \left. \frac{\partial \phi_i}{\partial s} \psi_i \right|_{B_1} - \int_{\Lambda_1} \sigma_{i_1}^s \frac{\partial \phi_i}{\partial s} \frac{\partial \psi_i}{\partial s} \, \mathrm{d}s = \beta \int_{\Lambda_1} \left[C_m \left(\frac{\partial \phi_i}{\partial t} - \frac{\partial \overline{\phi}_e}{\partial t} \right) \psi_i + i_{ion}(v, \mathbf{u}) \psi_i \right] \mathrm{d}s,$$

$$\sigma_{i_2}^s \left. \frac{\partial \phi_i}{\partial s} \psi_i \right|_{A_2} - \int_{\Lambda_2} \sigma_{i_2}^s \frac{\partial \phi_i}{\partial s} \frac{\partial \psi_i}{\partial s} \, \mathrm{d}s = \beta \int_{\Lambda_2} \left[C_m \left(\frac{\partial \phi_i}{\partial t} - \frac{\partial \overline{\phi}_e}{\partial t} \right) \psi_i + i_{ion}(v, \mathbf{u}) \psi_i \right] \mathrm{d}s,$$

$$\sigma_{i_3}^s \left. \frac{\partial \phi_i}{\partial s} \psi_i \right|_{A_3} - \int_{\Lambda_3} \sigma_{i_3}^s \frac{\partial \phi_i}{\partial s} \frac{\partial \psi_i}{\partial s} \, \mathrm{d}s = \beta \int_{\Lambda_3} \left[C_m \left(\frac{\partial \phi_i}{\partial t} - \frac{\partial \overline{\phi}_e}{\partial t} \right) \psi_i + i_{ion}(v, \mathbf{u}) \psi_i \right] \mathrm{d}s.$$

Multiplying each equation by $\pi R_{\Lambda_i}^2$, and applying (2.40) yields

$$(2.42) \quad \beta \int_{\Lambda} \pi R^2 C_m \left(\frac{\partial \phi_i}{\partial t} - \frac{\partial \overline{\phi}_e}{\partial t} \right) \psi_i + \pi R^2 i_{ion}(v, \mathbf{u}) \psi_i \, \mathrm{d}s = - \int_{\Lambda} \pi R^2 \sigma_i \frac{\partial \phi_i}{\partial s} \frac{\partial \psi_i}{\partial s} \, \mathrm{d}s,$$

where $R = R_{\Lambda_j}$ in Λ_j and $\sigma_i = \sigma_{i_j}$ in Λ_j for $j = 1, 2, 3$. Equation (2.42) implicitly enforces the internal boundary conditions due to Kirchoff's law at the branch point.

The weak form (2.42) may be directly included in the finite element approximation outlined in section 2.3.1, with the discrete finite element space defined as usual. The support of the basis function at a branching node is given by the union of all elements sharing that node. The resulting basis function is depicted in Figure 2.4(b). This results in an efficient and easy to implement finite element scheme that enforces current conservation at a fiber branch point.

2.6. Specialized conduction system coupled to a ventricular model. Equations (2.21a) and (2.21b) model a single specialized conduction system in a passive volume conductor, such as a bath. The equations are readily generalized for a fiber running along the endocardium or into the myocardium by adding a three-dimensional intracellular domain representing the myocardium. The composite equations for a fiber running through the myocardium are

$$(2.43) \qquad \beta \left(C_m \left(\frac{\partial \phi_i}{\partial t} - \frac{\partial \overline{\phi}_e}{\partial t} \right) + i_{ion}(v, \mathbf{u}) \right) = \sigma_i^s \frac{\partial^2 \phi_i}{\partial s^2} \qquad \text{in } \Lambda,$$

$$(2.44) \quad \beta_{im}\left(C_{im}\left(\frac{\partial\phi_{im}}{\partial t} - \frac{\overline{\partial\phi_e}}{\partial t}\right) + i_{ion}^{im}(v_{im}, \mathbf{u_{im}})\right) = \nabla\cdot(\sigma_{im}\nabla\phi_{im}) \quad \text{in } \Omega,$$

$$(2.45) \quad -\beta\pi R^2\left(C_m\left(\frac{\partial\phi_i}{\partial t} - \frac{\overline{\partial\phi_e}}{\partial t}\right) + i_{ion}(v, \mathbf{u})\right)\delta_\Lambda$$
$$-\beta_{im}\left(C_{im}\left(\frac{\partial\phi_{im}}{\partial t} - \frac{\partial\phi_e}{\partial t}\right) + i_{ion}^{im}(v_{im}, \mathbf{u_{im}})\right) = \nabla\cdot(\sigma_e\nabla\phi_e) \quad \text{in } \Omega,$$

where β_{im} is the surface to volume ratio, C_{im} is the capacitance per unit volume, and σ_{im} is the intracellular conductivity of the ventricular myocytes. i_{ion}^{im} is a nonlinear function representing the ionic currents across the cell membrane. ϕ_{im} is the intracellular potential of the ventricular myocytes, and $v_{im} = \phi_{im} - \phi_e$ is the transmembrane potential of the ventricular myocytes.

2.6.1. Purkinje-ventricular junction model. In the composite equations presented in the previous section, the specialized conduction system and the myocardium do not directly interact; they are only coupled via the extracellular potential. As the specialized conduction system is largely isolated from the myocardium, this is to be expected. However, at its terminal ends the specialized conduction system is coupled to the myocardium at discrete PV junctions. PV junctions are characterized as subendocardial sites where ventricular activation follows Purkinje activation, typically with a delay of approximately 5 ms. PV junctions are known to conduct in both directions but do so preferentially from Purkinje to myocardium. A model of PV junctions is required to provide a complete description of the specialized conduction system and its coupling to ventricular tissue.

A detailed electrophysiology model of a PV junction would make an interesting complement to this work. However, since we are interested in the specialized conduction system at the ventricular level, such a model would be unnecessarily detailed for our application. We use the simplest mathematical representation of the PV junction in the literature: a resistor model coupling discrete mesh nodes to the specialized conduction system introduced in [41] and refined to couple a mesh-independent volumetric region to the specialized conduction system in [2].

The PV junction is represented as a resistor connecting the intracellular space of the Purkinje fiber to a volumetric region, denoted Ω_{pvj}, in the myocardium. The average intracellular potential in the volumetric region is given by

$$\widehat{\phi_{im}} = \frac{1}{|\Omega_{pvj}|}\int_{\Omega_{pvj}}\phi_{im}\,\mathrm{d}\Omega,$$

where Ω_{pvj} is the volumetric region in the myocardium into which the specialized conduction system is coupled, $|\Omega_{pvj}|$ is its area and ϕ_{im} is the intracellular potential in the myocardium. The current through the PV junction is given by

$$(2.46) \quad I_{pvj}(\phi_i, \phi_{im}) = \frac{\phi_i(\mathbf{x}_{pvj}) - \widehat{\phi_{im}}}{R_{pvj}},$$

where $\phi_i(\mathbf{x}_{pvj})$ is the intracellular potential in the Purkinje fiber at the junction, and R_{pvj} is the resistance of the junction.

In previous work, current flow through the PV junctions to Purkinje fibers has been treated as a Robin boundary condition at the end of the fiber [2, 42]. However,

this is not in keeping with the micrograph studies of PV junctions [38] and the detailed three-dimensional model of [27], which show that Purkinje fibers are coupled by thin strands to transitional cells, with the transitional cell coupled in turn to the myocardium. The coupling strands can occur not only at their end points but also along the length of Purkinje fibers. Thus, the influence of PV junctions on the Purkinje fibers is treated as a source term in the Purkinje fiber equations. For each PV junction, (2.21a) is modified to give

$$(2.47) \qquad \beta \left(C_m \left(\frac{\partial \phi_i}{\partial t} - \frac{\partial \overline{\phi_e}}{\partial t} \right) + i_{ion}(v, \mathbf{u}) \right) = \sigma_i^s \frac{\partial^2 \phi_i}{\partial s^2} - \frac{I_{pvj}(\phi_i, \phi_{im})}{\pi R^2} \delta_{pvj},$$

where δ_{pvj} is a Dirac delta function centerd at the PV junction. The current flow through the PV junction to the myocardium is treated as a source term in the myocardial intracellular equation. Hence, for each PV junction, (2.44) is modified to give

$$(2.48)$$
$$\beta_{im} \left(C_{im} \left(\frac{\partial \phi_{im}}{\partial t} - \frac{\partial \phi_e}{\partial t} \right) + i_{ion}^{im}(v_{im}, \mathbf{u_{im}}) \right) = \nabla \cdot (\sigma_{im} \nabla \phi_{im}) + I_{pvj}^{vol}(\phi_i, \phi_{im}) \quad \text{in } \Omega,$$

where

$$(2.49) \qquad I_{pvj}^{vol}(\mathbf{x}) = \begin{cases} \frac{I_{pvj}}{|\Omega_{pvj}|}, & \mathbf{x} \in \Omega_{pvj}, \\ 0 & \text{otherwise.} \end{cases}$$

The two source terms balance total current flow to ensure conservation of current.

Equations (2.47) and (2.48) can be readily incorporated as explicit terms into the numerical scheme outlined in the previous section, and handled in a way similar to the ionic current terms.

3. Results. To demonstrate the model outlined above, we use a mesh of the rabbit ventricles incorporating the specialized conduction system. The techniques used to generate the mesh are described in detail in [6]. The mesh used here is less anatomically detailed than the original mesh described in [6] and omits the free-running portion of the Purkinje system. However, the mesh incorporates the major features of the specialized conduction system and the ventricles and is sufficiently detailed to demonstrate our bidomain model. In brief, the mesh was constructed as follows: A conforming tetrahedral mesh of the rabbit ventricles was generated from magnetic resonance images [5, 10]. The tetrahedral mesh had a relatively coarse average tetrahedra diameter of 480 μm. A custom tool was developed to allow the bundle of His and bundle branches to be added based on control points assigned by a user. Using this tool, the bundle of His and bundle branches were added to the model based on descriptions in the literature. A distal endocardial bound Purkinje system was generated using an L-system–based algorithm [17]. The specialized conduction system was projected onto the edges of the tetrahedral mesh for use with the finite element solution method presented here. PV junctions were placed uniformly over the distal endocardial bound Purkinje system. PV junctions were confined to the endocardial surface and not inserted transmurally into the wall.

As before, the Corrias model of rabbit cell electrophysiology was used to model ionic currents in the specialized conduction system [9], and the Mahajan–Shiferaw model was used to model ionic currents in the ventricles [23]. The radii of all specialized conduction system fibers were set to 100 μm. The resistance at PV junctions was

(a) 7 ms   (b) 14 ms   (c) 21 ms

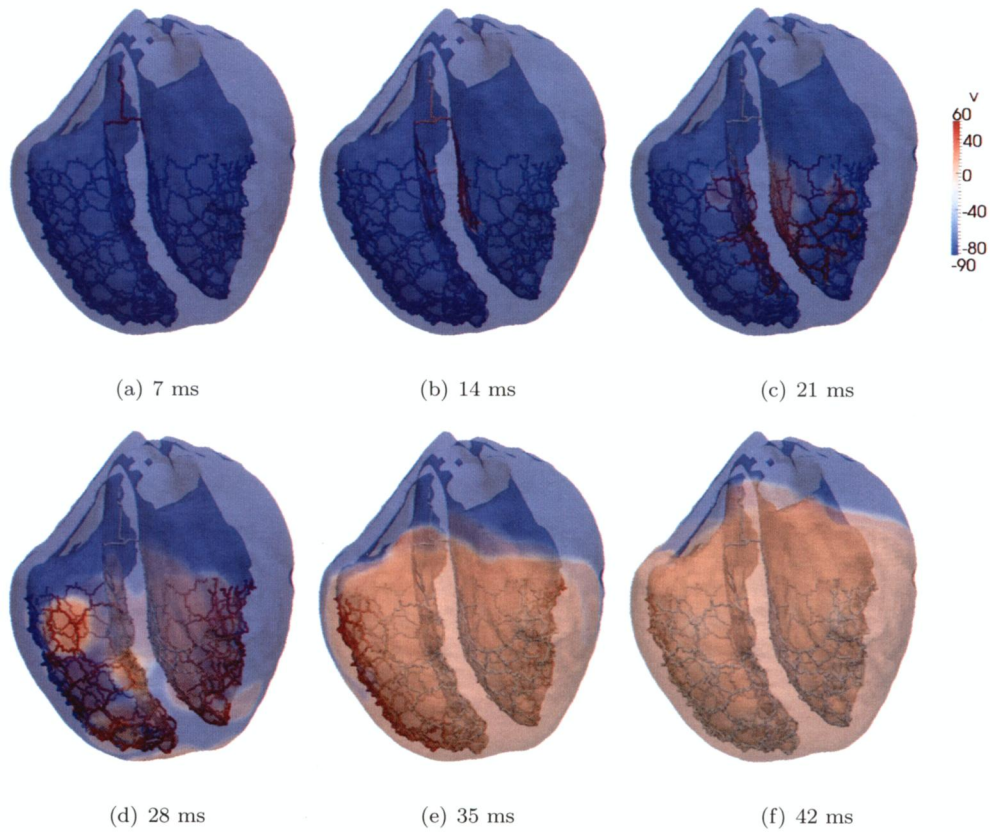(d) 28 ms   (e) 35 ms   (f) 42 ms

FIG. 3.1. *Activation in the specialized conduction system and the ventricles after stimulation of the bundle of His. The ventricles are shown as semitransparent to allow the specialized conduction system to be seen; the left ventricle is shown to the right. Color indicates transmembrane potential. Captions indicate time since the bundle of His was stimulated.*

set to 20 $M\Omega$, as described in [41]. The volumetric region in the myocardium linked to each PV junction was a hemisphere of radius 1mm. Intracellular conductivity in the specialized conduction system was set to 4 mS cm^{-1} to ensure sufficiently fast propagation in the specialized conduction system. The remaining parameters, governing electrical propagation in the myocardium, are as in [39]. Simulation code was implemented using the libMesh finite element library [21].

3.1. Ventricular activation. Activation of the ventricles after stimulation of the bundle of His is shown in Figure 3.1. The proximal end of the bundle of His was stimulated intracellularly to induce propagation into the specialized conduction system. The resulting activation sequence proceeded though the septum, then from apex to base. Activity proceeded from the endocardium to the epicardium throughout the myocardium.

3.2. Defibrillation strength shock response. The principal advantage of the bidomain model presented here compared to monodomain models is that it allows the effect of externally applied fields on the specialized conduction system to be investigated. To test this capability an externally applied electric field of strength 2 V/cm was applied for 1 ms to the isolated specialized conduction system. The simulation

was repeated three times, with the field applied along each principal axis in turn. Figure 3.2 shows activation in the isolated specialized conduction system 1 ms after the application of the electric field in each case. Excitation of the conduction system varied strongly depending on the direction of the electric field. In each case, depolarization and hyperpolarization occurred at numerous distinct sites throughout the specialized conduction system as a result of virtual electrode polarization. Smaller fibers were more strongly polarized than larger fibers by virtual electrodes. The effect of the electric field was particularly prominent when the angle of incidence between specialized conduction system fibers and the field was small. Due to the orientation of the bundle branches and bundle of His, this meant that the system was most strongly polarized by the shock oriented along the z-axis.

4. Summary and model limitations. The major contribution of this study is the development of a one-dimensional bidomain Purkinje fiber model that accounts for the interaction of Purkinje fibers with the extracellular field in the heart. The model is thus suitable for use in defibrillation studies as well as electrical propagation studies. The one-dimensional nature of the model gives it the efficiency required for implementation of large specialized conduction system networks and for its use in ventricular simulations. A further contribution is the introduction of a numerical method to enforce Kirchoff's law at Purkinje fiber branch points within a standard finite element framework. The branch point solution method does not rely on the use of higher order basis functions or the use of the finite volume method as required by previous work. Using a geometric representation of the ventricular specialized conduction system, bidomain simulations were performed to demonstrate ventricular activation sequence resulting from sinus rhythm and the impact of an externally applied shock on the system. The model demonstrated physiologically realistic activation sequences, with epicardial breakthrough locations similar to those observed experimentally. The model showed that the strength of the externally applied shock and the angle of incidence of specialized conduction system fibers to the direction of the external field determine the effect of the shock.

The starting point for the one-dimensional model presented here did not include an explicit representation of the connective tissue sheath that surrounds specialized conduction system fibers [13]. The sheath is largely made up of collagen, with smaller amounts of elastin and other materials. The sheath serves as a structural support for specialized conduction system fibers and electrically isolates them from surrounding myocardial tissue. If the conductivity of the collagen sheath differs significantly from the surrounding myocardial tissue or bath, then its presence may play a role in how the specialized conduction system behaves when exposed to externally applied electrical fields. The techniques presented here for reducing a three-dimensional fiber to an idealized one-dimensional fiber present an obvious starting point for incorporating the collagen sheath into a one-dimensional model of specialized conduction system fibers.

Appendix. In this appendix, we prove existence and uniqueness of the solution of the time-discrete weak form (2.27) derived in section 2.3 with Dirichlet data. The requirement for applying Dirichlet boundary conditions stems from the degeneracy of the standard bidomain equations that result in solutions being defined only up to a constant. We begin by proving that the averaging operator (2.12) is a bounded linear operator.

LEMMA A.1. *Let $\alpha \in (-1, 1)$; the linear mapping $u \to \bar{u}$ from $H_\alpha^1(\Omega)$ to $L^2(\Lambda)$ is bounded.*

(a) x-axis 1 ms postshock.

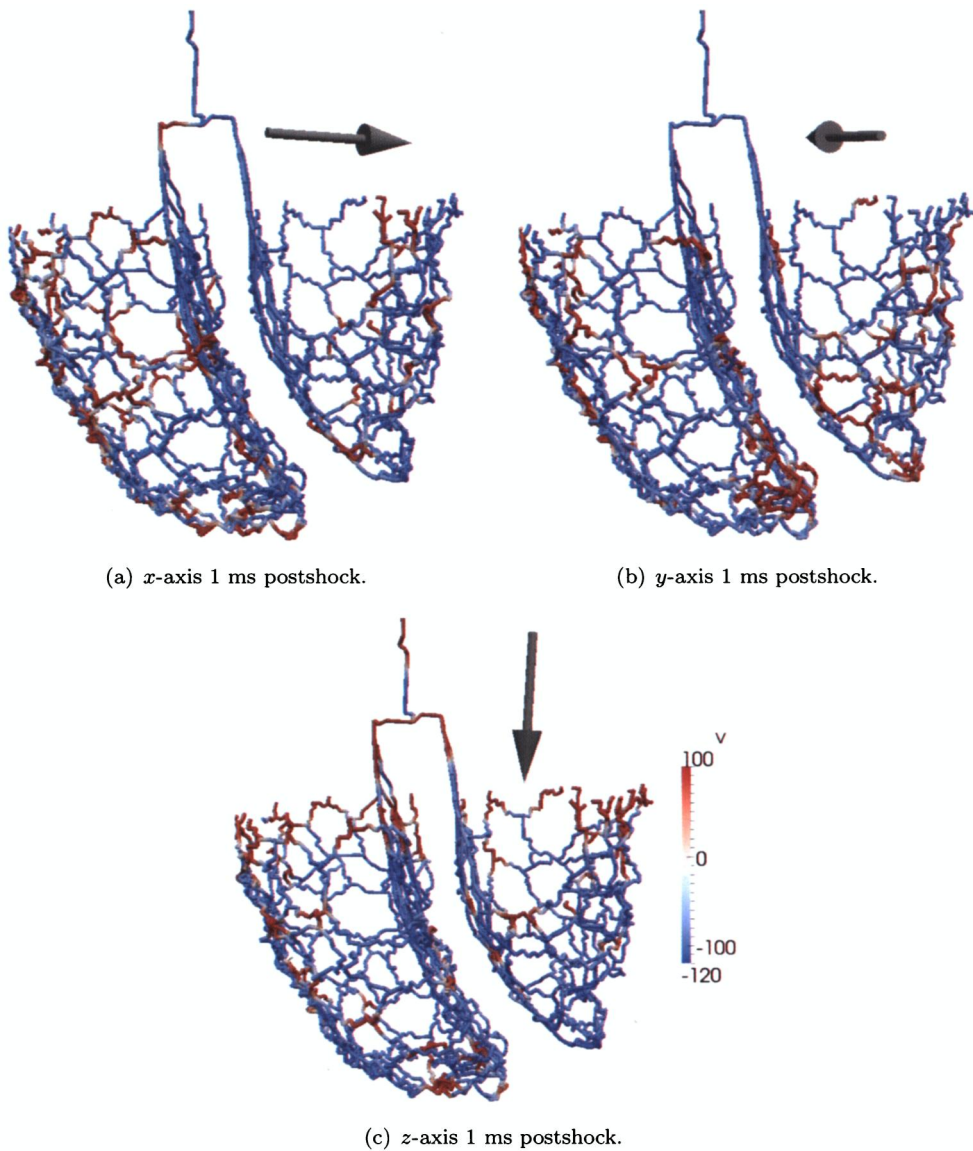(b) y-axis 1 ms postshock.

(c) z-axis 1 ms postshock.

FIG. 3.2. *Activation in the specialized conduction 1 ms after a 2 V/cm electric field was applied for 1 ms in each of the three principal axes. The color scale indicates the transmembrane potential in the system. Arrows indicate direction of the applied electric field.*

Proof. For any $u \in C^\infty(\Omega)$,

$$(A.1) \quad \int_\Lambda \overline{u}(s)^2 \, ds = \int_\Lambda \left(\frac{1}{\pi R^2} \int_0^{2\pi} \int_0^R ur \, dr d\theta \right)^2 ds$$

$$(A.2) \quad \leq \int_\Lambda \left(\frac{1}{\pi R^2} \int_0^{2\pi} \int_0^R u^2 r^{2\alpha} r^{2-2\alpha} \, dr d\theta \right) ds$$

$$(A.3) \quad \leq \frac{R^{-2\alpha}}{\pi} \|u\|^2_{L^2_\alpha(\Omega^R)} \leq \frac{R^{-2\alpha}}{\pi} \|u\|^2_{H^1_\alpha(\Omega)}.$$

Thus, $\overline{u}$ is a bounded linear operator from $H^1_\alpha(\Omega)$ to $L^2(\Lambda)$.   □

We now introduce the key theorem that is used to show well-posedness of the problem. The theorem is a minor modification of Theorem 5.1 of [12], and the material in this section is largely reproduced from that paper.

Consider a pair of spaces V_1, V_2 of real functions on Ω, and a space $\hat{V}$ of real functions on Λ. Let $A : V_1 \times V_2 \to \mathbb{R}$, $\hat{A} : \hat{V} \times \hat{V} \to \mathbb{R}$ be the bilinear forms

$$(A.4) \qquad A(u, v) = \int_\Omega A_1 \nabla u \cdot \nabla v \mathrm{dx} + \int_\Omega A_0 uv \mathrm{dx},$$

$$(A.5) \qquad \hat{A}(\hat{u}, \hat{v}) = \int_\Lambda \hat{A}_1 \frac{\mathrm{d}\hat{u}}{\mathrm{d}s} \frac{\mathrm{d}\hat{v}}{\mathrm{d}s} \mathrm{ds} + \int_\Lambda \hat{A}_0 \hat{u}\hat{v} \mathrm{ds},$$

where A_1, $A_0 \in L^\infty(\Omega)$ and $\hat{A}_1$, $\hat{A}_0 \in L^\infty(\Lambda)$. Let $\Pi : V_1 \to L^2(\Lambda)$ be a continuous linear operator, and let two continuous functionals $B : V_2 \to \mathbb{R}$, $\hat{B} : \hat{V} \to \mathbb{R}$ be given.

Then consider following the abstract problem: Find $(u, \hat{u}) \in V_1 \times \hat{V}$ such that

$$(A.6) \qquad A(u, v) + \int_\Lambda \kappa(\Pi u - \hat{u})v \mathrm{ds} = B(v) \quad \forall v \in V_2,$$

$$(A.7) \qquad \hat{A}(\hat{u}, \hat{v}) - \int_\Lambda \kappa(\Pi u - \hat{u})\hat{v} \mathrm{ds} = \hat{B}(\hat{v}) \quad \forall \hat{v} \in \hat{V},$$

where $\kappa \in L^\infty(\Lambda)$.

We now set $V_1 = \{u \in H^1_\alpha(\Omega) : u|_\Gamma = 0\}$, $V_2 = \{u \in H^1_{-\alpha}(\Omega) : u|_\Gamma = 0\}$ for some $\Gamma \subset \partial\Omega$ and $\hat{V} = \{\hat{u} \in H^1(\Lambda) : \hat{u}(s_2) = 0\}$. Consider the spaces $\mathbf{V}_1 = V_1 \times \hat{V}$, $\mathbf{V}_2 = V_2 \times \hat{V}$; for every $\mathbf{u} = (u, \hat{u}) \in \mathbf{V}_1$ and $\mathbf{v} = (v, \hat{v}) \in \mathbf{V}_2$, define the bilinear form and linear functional

$$(A.8) \qquad a(\mathbf{u}, \mathbf{v}) = A(u, v) + \hat{A}(\hat{u}, \hat{v}) + \int_\Lambda \kappa(\Pi u - \hat{u})(v - \hat{v}) \mathrm{ds},$$

$$(A.9) \qquad F(\mathbf{v}) \overset{.}{=} B(v) + \hat{B}(\hat{v}),$$

with $B \in V_1'$, $\hat{B} \in \hat{V}'$.

THEOREM A.2. *Let $A_i \in L^\infty(\Omega)$, $\hat{A}_i \in L^\infty(\Lambda)$ and assume that $A_0 \geq 0$, $A_1 \geq A_{min}$, $\hat{A}_0 \geq 0$, $\hat{A}_1 \geq A_{min}$, with $A_{min} > 0$ a constant and $i = 0, 1$. Let $\Pi : H^1_\alpha(\Omega) \to L^2(\Lambda)$, a, and F be, respectively, a bounded linear operator, the bilinear form (A.8), and the linear functional (A.9), where $B \in V_1'$, $\hat{B} \in \hat{V}'$. Then there is a constant $\delta \in (0, 1)$ and a positive function $\kappa_{max}(\alpha)$, such that if $\alpha \in (0, \delta)$ and $||\kappa||_\infty < \kappa_{max}(\alpha)$, there exists a unique $\mathbf{u} \in \mathbf{V}_1$ such that*

$$a(\mathbf{u}, \mathbf{v}) = F(\mathbf{v}) \qquad \forall \mathbf{v} \in \mathbf{V}_2.$$

Moreover, there is a positive number $C = C(\alpha, A_{min}, ||A_i||_\infty, ||\hat{A}_i||_\infty, ||\kappa||_\infty)$ such that

$$(A.10) \qquad ||\mathbf{u}||_{\mathbf{V}_1} \leq C||F||_{\mathbf{V}_2'}.$$

Proof. The proof is identical to that for Theorem 5.1 of [12] except for two minor modifications to Lemma 4.2 of [12]. The Dirichlet boundary condition on V_1 is used to prove that $\sup_{u \in V_1} |A(u, v)| > 0$, and Poincaré's inequality is used to show that $A(u, v) \geq M||u||^2_{V_1}$ (equation (4.21) of [12]) holds with $M = \frac{(A_1 - 2\delta C_3)R^{2\alpha}}{(1 + C_P^2)\mathrm{diam}(\Omega)^{2\alpha}}$, where $0 < \delta < A_1/(2C_3)$, C_p is the Poincaré constant, and $C_3 > 0$ is the constant given in Theorem 4.3 of [12].   □

To apply Theorem A.2 to our time-discrete problem, first we observe that (2.22) is of the same form as (A.8), and (2.23) is of the same form as (A.9). Second, we observe that β, C_m, σ_i^s and σ_e are all real constants greater than zero and that our averaging operator is bounded and linear. We assume that the data from the previous time-step $(\phi_e^{n-1}, \phi_i^{n-1})$ exist in the appropriate space. For the spaces $\mathbf{V}_1 = V_1 \times \hat{V}$, $\mathbf{V}_2 = V_2 \times \hat{V}$ all the prerequisites of Theorem A.2 are satisfied. Applying the theorem we conclude that at each time-step there exists a constant $\delta \in (0,1)$ and a positive function $\kappa_{max}(\alpha)$, such that if $\alpha \in (0, \delta)$ and $\|\kappa\|_\infty < \kappa_{max}(\alpha)$, there exists a unique $(\phi_e^n, \phi_i^n) \in \mathbf{V}_1$ such that

$$a((\phi_e^n, \phi_i^n), (\psi_e, \psi_i)) = F(\psi_e, \psi_i) \qquad \forall (\psi_e, \psi_i) \in \mathbf{V}_2.$$

Moreover, there is a positive number C such that

(A.11)
$$\|(\phi_e^n, \phi_i^n)\|_{\mathbf{V}_1} \le C\|F\|_{\mathbf{V}_2'}.$$

We conclude that, at each time-step, solutions to the time-discrete version of our problem exist in the space $\mathbf{V}_1$, are unique, and are bounded. This assumes that the data from the previous time-step are also well-posed. Unfortunately, extending these results to the full time-continuous system of equations would require energy estimates for (ϕ_e^n, ϕ_i^n). This will require nonstandard techniques due to the use of the function space H_α^1, and its test space $H_{-\alpha}^1$, and is beyond the scope of this paper. Furthermore, the nonlinearity of the ionic current term would have to be addressed. This could potentially be achieved using the techniques presented in [3] and [8].

REFERENCES

[1] S. Abboud, O. Berenfeld, and D. Sadah, *Simulation of high-resolution QRS complex using a ventricular model with a fractal conduction system. Effects of ischemia on high-frequency QRS potentials*, Circ. Res., 68 (1991), pp. 1751–1760.

[2] A. Azzouzi, Y. Coudiere, and R. Turpault, *A mathematical model of the ventricular conduction system*, in Proceedings of the International Conference of Numerical Analysis and Applied Mathematics (ICNAM), AIP Conf. Proc. 1281, Springer, Berlin, 2010, pp. 403–406.

[3] M. Bendahmane and K. H. Karlsen, *Analysis of a class of degenerate reaction-diffusion systems and the bidomain model of cardiac tissue*, Netw. Heterog. Media, 1 (2006), pp. 185–218.

[4] O. Berenfeld and J. Jalife, *Purkinje-muscle reentry as a mechanism of polymorphic ventricular arrhythmias in a 3-dimensional model of the ventricles*, Circ. Res., 82 (1998), pp. 1063–1077.

[5] M. J. Bishop, G. Plank, R. A. B. Burton, J. E. Schneider, D. J. Gavaghan, V. Grau, and P. Kohl, *Development of an anatomically detailed MRI-derived rabbit ventricular model and assessment of its impact on simulations of electrophysiological function*, Am. J. Physiol. Heart Circ. Physiol., 298 (2010), pp. H699–H718.

[6] R. Bordas, K. Gillow, Q. Lou, I. R. Efimov, D. Gavaghan, P. Kohl, V. Grau, and B. Rodriguez, *Rabbit-specific ventricular model of cardiac electrophysiological function including specialized conduction system*, Prog. Biophys. Mol. Bio., 107 (2011), pp. 90–100.

[7] P. Colli-Franzone and L. Pavarino, *A parallel solver for reaction-diffusion systems in computational electrocardiology*, Math. Models Methods Appl. Sci., 14 (2004), pp. 883–911.

[8] P. COLLI-FRANZONE AND G. SAVARE, *Degenerate evolution systems modeling the cardiac electric field at micro-and macroscopic level*, in Evolution Equations, Semigroups and Functional Analysis, Progr. Nonlinear Differential Equations Appl. 50, Birkhäuser, Basel, 2002, pp. 49–78.

[9] A. CORRIAS, W. GILES, AND B. RODRIGUEZ, *Ionic mechanisms of electrophysiological properties and repolarization abnormalities in rabbit Purkinje fibers*, Am. J. Physiol. Heart Circ. Physiol., 300 (2011), pp. H1806–H1813.

[10] A. CORRIAS, X. JIE, L. ROMERO, M. J. BISHOP, M. BERNABEU, E. PUEYO, AND B. RODRIGUEZ, *Arrhythmic risk biomarkers for the assessment of drug cardiotoxicity: From experiments to computer simulations*, Phil. Trans. R. Soc. A, 368 (2010), pp. 3001–3025.

[11] C. D'ANGELO, *Multiscale Modelling of Metabolism and Transport Phenomena in Living Tissues*, Ph.D. Thesis, École Polytechnique Fédérale de Lausanne, Lausanne, Switzerland, 2007.

[12] C. D'ANGELO AND A. QUARTERONI, *On the coupling of 1D and 3D diffusion-reaction equations. Application to tissue perfusion problems*, Math. Models Methods Appl. Sci., 18 (2008), pp. 1481–1504.

[13] W. DUN AND P. A. BOYDEN, *The Purkinje cell; 2008 style*, J. Mol. Cell. Cardiol., 45 (2008), pp. 617–624.

[14] R. FITZHUGH, *Impulses and physiological states in theoretical models of nerve membrane*, Biophys. J., 1 (1961), pp. 445–466.

[15] C. S. HENRIQUEZ, *Simulating the electrical behavior of cardiac tissue using the bidomain model*, Crit. Rev. Biomed. Eng., 21 (1993), pp. 1–77.

[16] C. S. HENRIQUEZ AND R. PLONSEY, *Simulation of propagation along a cylindrical bundle of cardiac tissue. 1. Mathematical formulation*, IEEE Trans. Bio.-Med. Eng., 37 (1990), pp. 850–860.

[17] T. IJIRI, T. ASHIHARA, T. YAMAGUCHI, K. TAKAYAMA, T. IGARASHI, T. SHIMADA, T. NAMBA, R. HARAGUCHI, AND K. NAKAZAWA, *A procedural method for modeling the Purkinje fibers of the heart*, J. Physiol., 58 (2008), pp. 481–486.

[18] J. KEENER AND K. BOGAR, *A numerical method for the solution of the bidomain equations in cardiac tissue*, Chaos, 8 (1998), pp. 234–240.

[19] J. KEENER AND J. SNEYD, *Mathematical Physiology*, Springer, New York, 1998.

[20] K. KIM AND M. SUNG, *Symmetric quadrature formulas over a unit disk*, J. Comput. Appl. Math., 4 (1997), pp. 179–192.

[21] B. S. KIRK, J. W. PETERSON, R. H. STOGNER, AND G. F. CAREY, *libMesh: A c++ library for parallel adaptive mesh refinement/coarsening simulations*, Eng. Comput.-Germany, 22 (2006), pp. 237–254.

[22] M. LORANGE AND R. M. GULRAJANI, *A computer heart model incorporating anisotropic propagation*, J. Electrocardiol., 26 (1993), pp. 245–261.

[23] A. MAHAJAN, Y. SHIFERAW, D. SATO, A. BAHER, R. OLCESE, L.-H. XIE, M.-J. YANG, P.-S. CHEN, J. G. RESTREPO, A. KARMA, A. GARFINKEL, Z. QU, AND J. N. WEISS, *A rabbit ventricular action potential model replicating cardiac dynamics at rapid heart rates*, Biophys. J., 94 (2008), pp. 392–410.

[24] J. NEU AND W. KRASSOWSKA, *Homogenization of syncytial tissues*, Crit. Rev. Biomed. Eng., 21 (1993), pp. 137–199.

[25] R. PLONSEY, *Bioelectric sources arising in excitable fibers (ALZA lecture)*, Ann. Biomed. Eng., 16 (1988), pp. 519–546.

[26] A. POLLARD AND R. C. BARR, *The construction of an anatomically based model of the human ventricular conduction system*, IEEE. Trans. Bio.-Med. Eng., 37 (1990), pp. 1173–1185.

[27] A. POLLARD AND W. CANTRELL, *Action potential propagation in a bidomain model of the discrete Purkinje-ventricular junction*, in Proceedings of the 18th Annual Conference of the IEEE Engineering in Medicine and Biology Society, Vol. 3, IEEE Press, Piscataway, NJ, 1996, pp. 1244–1245.

[28] A. QUARTERONI AND A. VALLI, *Domain Decomposition Methods for Partial Differential Equations*, Oxford University Press, Oxford, UK, 1999.

[29] G. RICHARDSON AND S. J. CHAPMAN, *Derivation of the bidomain equations for a beating heart with a general microstructure*, SIAM J. Appl. Math., 71 (2011), pp. 657–675.

[30] B. RODRIGUEZ, L. LI, J. EASON, I. EFIMOV, AND N. A. TRAYANOVA, *Differences between left and right ventricular chamber geometry affect cardiac vulnerability to electric shocks*, Circ. Res., 97 (2005), pp. 168–175.

[31] B. RODRIGUEZ, B. TICE, J. EASON, F. AGUEL, AND N. A. TRAYANOVA, *Cardiac vulnerability to electric shocks during phase 1A of acute global ischemia*, Heart Rhythm, 1 (2004), pp. 695–703.

[32] M. M. SCHEINMAN, *Role of the His-Purkinje system in the genesis of cardiac arrhythmia*, Heart Rhythm, 6 (2009), pp. 1050–1058.

[33] M. SCHOENBERG, G. DOMINGUEZ, AND H. FOZZARD, *Effect of diameter on membrane capacity and conductance of sheep cardiac Purkinje fibers*, J. Gen. Physiol., 65 (1975), pp. 441–458.

[34] R. SCOTT, *Finite-element convergence for singular data*, Numer. Math., 21 (1973), pp. 317–327.

[35] M. SILVERMAN, D. GROVE, AND C. UPSHAW, JR., *Why does the heart beat? The discovery of the electrical system of the heart*, Circulation, 113 (2006), pp. 2775–2781.

[36] K. SIMELIUS, J. NENONEN, AND B. HORACEK, *Modeling cardiac ventricular activation*, Inter. J. Bioelectromagnetism, 3 (2001), pp. 51–58.

[37] K. H. W. J. TEN TUSSCHER AND A. V. PANFILOV, *Modelling of the ventricular conduction system*, Prog. Biophys. Mol. Bio., 96 (2008), pp. 152–170.

[38] J. TRANUM-JENSEN, A. A. M. WILDE, J. T. VERMEULEN, AND M. J. JANSE, *Morphology of electrophysiologically identified junctions between Purkinje fibers and ventricular muscle in rabbit and pig hearts*, Circ. Res., 69 (1991), pp. 429–437.

[39] N. A. TRAYANOVA, J. EASON, AND F. AGUEL, *Computer simulations of cardiac defibrillation: A look inside the heart*, Comput. Visual Sci., 4 (2002), pp. 259–270.

[40] E. J. VIGMOND, F. AGUEL, AND N. A. TRAYANOVA, *Computational techniques for solving the bidomain equations in three dimensions*, IEEE Trans. Bio.-Med. Eng., 49 (2002), pp. 1260–1269.

[41] E. J. VIGMOND AND C. CLEMENTS, *Construction of a computer model to investigate sawtooth effects in the Purkinje system*, IEEE Trans. Bio.-Med. Eng., 54 (2007), pp. 389–398.

[42] E. J. VIGMOND, F. VADAKKUMPADAN, V. GUREV, H. AREVALO, M. DEO, G. PLANK, AND N. A. TRAYANOVA, *Towards predictive modelling of the electrophysiology of the heart*, Exp. Physiol., 94 (2009), pp. 563–577.

[43] T. WASHIO, J. I. OKADA, AND T. HISADA, *A parallel multilevel technique for solving the bidomain equation on a human heart with Purkinje fibers and a torso model*, SIAM J. Sci. Comput., 30 (2008), pp. 2855–2881.

[44] J. P. WHITELEY, *An efficient numerical technique for the solution of the monodomain and bidomain equations*, IEEE Trans. Bio.-Med. Eng., 53 (2006), pp. 2139–2147.